

1 Neutron-Neutron Correlations in the Photofission of U-238

2 J. Burggraf, D.S. Dale, and T. Forest
3

4 *Department of Physics,*
5 *Idaho State University, Pocatello, ID 83201*

6 G. Warren, S. Stave, S. Behling, and E. Church
7

8 *Pacific Northwest National Laboratory, PO Box 999, Richland, Washington 99352*

(Dated: July 10, 2019)

9 **Background:** In the fission of actinides, the nearly back-to-back motion of the fission fragments has a strong
10 effect on the kinematics of fission neutrons. This leads to a favoring of opening angles near 0° and 180° in the
11 neutron-neutron (n-n) opening angle distributions of correlated neutron pairs from the same fission event.

12 **Purpose:** To measure the n-n opening angle and energy correlations in the photofission of ^{238}U . As of this
13 writing, measurements of correlated n-n opening angle distributions have been reported only for the spontaneous
14 and neutron-induced fission of actinides. This work is the first to report such a measurement using photofission
15 and will provide useful experimental input for photofission models used in codes such as MCNP and FREYA.

16 **Method:** Fission is induced using bremsstrahlung photons produced via a low duty factor, pulsed, linear electron
17 accelerator. The bremsstrahlung photon beam impinges upon a ^{238}U target that is surrounded by a large neutron
18 scintillation detection system capable of measuring particle position and time of flight, from which n-n opening
19 angle and energy are measured. Neutron-neutron angular correlations are determined by taking the ratio between
20 a correlated neutron distribution and an uncorrelated neutron distribution formed by the pairing of neutrons pro-
21 duced during different beam pulses. This analysis technique greatly diminishes effects due to detector efficiencies,
22 acceptance, and experimental drifts.

23 **Results:** The angular correlation of neutrons from the photofission of ^{238}U shows a high dependence on neutron
24 energy as well as a dependence on the angle of the emitted neutrons with respect to the incoming photon beam.
25 Angular correlations were also measured using neutrons from the spontaneous fission of ^{252}Cf , showing good
26 agreement with past measurements.

27 **Conclusions:** The measured angular correlations reflect the underlying back-to-back nature of the fission frag-
28 ments. An anomalous decline in n-n yield was observed for opening angles near 180° for ^{238}U .

29 CONTENTS

30 I. Overview of Neutron-Neutron Angular
31 Correlations in Fission
32 A. Theoretical Basis
33 B. Past Measurements: Spontaneous and
34 Neutron Induced Fission
35 C. Considerations for Photofission

36 II. Experimental Setup
37 A. Detectors
38 B. Detector Shielding
39 C. Bremsstrahlung Photon Beam
40 D. DU Target
41 E. Electronics

42 III. Measurement Techniques
43 A. Particle Time of Flight and Energy
44 Determination
45 B. Particle Position Reconstruction
46 C. Measurements with ^{252}Cf

47 IV. Analysis
48 A. Cancelation of Detector Efficiencies, Drifts,
49 and Geometric Phase Space
50 B. Subtraction of Accidental Coincidences

51 V. Potential sources of error

52 A. Correlated versus uncorrelated n-n energy
53 distribution

54 B. Detector Cross-talk

55 1. Simulation of Detector Cross-talk

56 C. Neutron Scattering within the Target

57 VI. Results

58 A. n-n angular correlation versus neutron
59 energy

60 B. Considering θ_{abs}

61 VII. Concluding Remarks

62 VIII. Acknowledgments

63 References

7 I. OVERVIEW OF NEUTRON-NEUTRON 8 ANGULAR CORRELATIONS IN FISSION

9 The fission process is characterized by the emission of
10 neutrons. Neutron emission in fission can be classified
11 into two categories depending on the time of emission:
12 delayed and prompt. Prompt fission neutrons are de-
13 fined as neutrons that are emitted either immediately

71 after ($< 10^{-14}$ seconds) fission, or during the scission
 72 of the nucleus, and account for $\sim 99\%$ of neutron emis-
 73 sion [1]. Delayed neutrons are not relevant to the present
 74 work because they account for only $\sim 1\%$ of total neutron
 75 emission in actinide photofission [1], and they are emit-
 76 ted milliseconds to minutes after fission which is well out-
 77 side the neutron acceptance timing window of the present
 78 work.

79 Prompt fission neutron production occurs by means of
 80 two distinct mechanisms. The dominant mechanism is
 81 neutron emission from the fully accelerated fragments.
 82 The second mechanism, referred to as *early* or *scission*
 83 neutron emission, is the emission of neutrons during ei-
 84 ther the scission of the nucleus or the acceleration of the
 85 fission fragments. A large number of past studies have
 86 established that the majority of prompt fission neutrons
 87 (80%–98%) are emitted from the fully accelerated frag-
 88 ments, while scission neutrons account for the remaining
 89 2%–20% percent [2]. The nature of scission neutrons has
 90 remained elusive since their first tentative observation in
 91 1962 by Bowman *et al.* [3].

92 A. Theoretical Basis

93 The neutron-neutron (n-n) opening angle distribution
 94 of correlated neutron pairs, as seen in the lab frame, is
 95 widely used for the quantification of n-n angular correla-
 96 tions. Angular correlations in fission neutrons arise due
 97 to the kinematics of the fission fragments. It has been
 98 shown that neutrons released from the fully accelerated
 99 fission fragments are evaporated isotropically in the frag-
 100 ment's rest frame, and are emitted at speeds compara-
 101 ble to that of the fragments themselves [4]. This leads
 102 to the well-known U-shaped distribution in neutron-
 103 neutron opening angle (θ_{nn}), which has been reported
 104 in studies of neutron-induced, spontaneous, and in this
 105 work, photofission. An example of a typical θ_{nn} distri-
 106 bution is seen in Fig. 1.

107 The U-shaped distribution of θ_{nn} can be understood
 108 as the result of the boost provided to the neutrons by the
 109 fission fragments in binary fission. Due to the conserva-
 110 tion of momentum, the fully accelerated fission fragments
 111 are traveling nearly back-to-back, and neutrons emitted
 112 from different fragments are boosted in opposite direc-
 113 tions, whereas neutrons emitted from the same fragment
 114 are boosted in the same direction. Thus, because the
 115 velocities of the fission fragments are large enough to ac-
 116 count for a significant portion of the kinetic energy of
 117 fission neutrons, neutron pairs emitted from the acceler-
 118 ated fragments exhibit a favoring of opening angles near
 119 0° if emitted from the same fragment and 180° if emitted
 120 from different fragments, and consequently, a suppression
 121 of opening angles near 90°.

122 The favoring of large and small n-n opening angles
 123 shows a strong dependence on neutron energy. Neutrons
 124 with higher energy are more likely to have been emitted
 125 along the same direction as the fission fragments and are

126 therefore expected to favor large and small opening an-
 127 gles. The θ_{nn} distribution and its dependence on neutron
 128 energy are expected to shed light on several fundamental
 129 aspects of the fission process including the neutron mul-
 130 tiplicity distributions associated with the light and heavy
 131 fission fragments, the nuclear temperatures of the fission
 132 fragments, and the mass distribution of the fission frag-
 133 ments as a function of energy released. In addition, the
 134 unique kinematics of fission and the resulting n-n corre-
 135 lations have the potential to be the basis for a new tool
 136 to characterize fissionable materials [5].

137 B. Past Measurements: Spontaneous and Neutron 138 Induced Fission

139 The first measurement of the angular correlation
 140 among coincident neutrons from fission was performed
 141 by Debenedetti *et al.* [6] in 1948 from neutron induced
 142 fission of ^{235}U . The next measurement of this type was
 143 performed by Pringle and Brooks in 1975 [7], in which
 144 neutrons emitted from the spontaneous fission (SF) of
 145 ^{252}Cf were found to have high coincidence rates at small
 146 opening angles near 0° and large opening angles near
 147 180°. In order to produce a result that is insensitive to
 148 the effects of detector geometry and efficiency, the present
 149 work uses techniques similar to those used in reference [7],
 150 in which a ratio is taken between a correlated opening an-
 151 gle distribution and an uncorrelated opening angle distri-
 152 bution. Measurements of n-n angular correlation in the
 153 SF of ^{252}Cf , the most studied case of correlated neutron
 154 emission in fission, were also performed in the present
 155 work and show good agreement with past measurements,
 156 as seen in Fig. 1. Correlated n-n measurements have also
 157 been performed using thermal neutron induced fission of
 158 ^{235}U , ^{233}U , and ^{239}Pu [11].

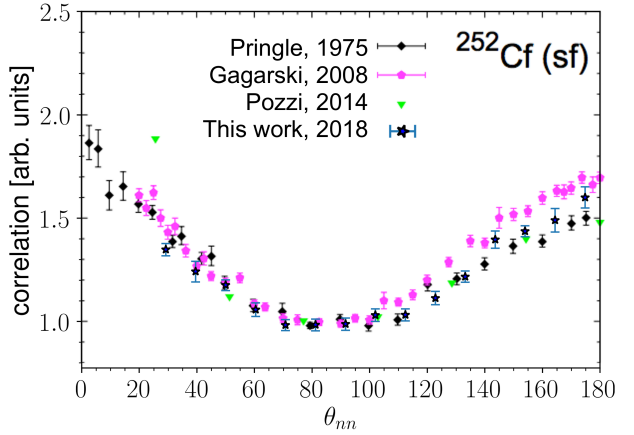


FIG. 1: θ_{nn} distribution from the spontaneous fission of ^{252}Cf . The minimum neutron energy cut-off for Pringle [7], Gagarski [10], and Pozzi [12] is 0.425 MeV, 0.425 MeV, and 0.7 MeV, respectively, and for this work is 0.4 MeV.

161 C. Considerations for Photofission

162 The photofission reaction occurs during the de-
 163 excitation of a nucleus after the absorption of a pho-
 164 ton. For photon energies between 6 and 25 MeV, this
 165 absorption occurs primarily via the giant dipole reso-
 166 nance (GDR) excitation. One distinct and useful as-
 167 pect of photofission, relative to neutron-induced fission,
 168 is the low transfer of angular momentum to the nucleus,
 169 which gives rise to a simpler set of selection rules for
 170 the transfer of angular momentum. For the photofis-
 171 sion of even-even nuclei, excitation occurs primarily via
 172 electric dipole transitions, and to a lesser extent electric
 173 quadrupole transitions, which gives rise to anisotropies
 174 in the fission fragment angular distribution that are far
 175 more pronounced than for other types of fission [13].
 176 These anisotropies are expressed in the angular distribu-
 177 tion of emitted neutrons. For these reasons, photofission
 178 is increasingly being used as a means to study sub-nuclear
 179 structures and the fundamentals of the fission process.
 180 Such studies are needed in order to dial in various model
 181 parameters required for an accurate theoretical descrip-
 182 tion of the fission process.

183 II. EXPERIMENTAL SETUP

184 This experiment was carried out at the Idaho Accelerator Center (IAC), using their short-pulsed linear accelerator, which is an L-band frequency (1300 MHz) electron linear accelerator. See section II C for the accelerator parameters used during the experiment. Figure 2 shows a 189 top-down diagram of the experimental arrangement.

190 A. Detectors

191 The detection system measures neutron position and 192 time of flight (ToF), which is defined as the time taken for 193 a particle to travel from the fission target to a detector. 194 The purpose of the ToF measurement is to determine the 195 kinetic energy of detected neutrons and to distinguish 196 between photons and neutrons. The detection system's 197 positional precision is ± 9 cm, which gives an average 198 angular precision of $\pm 6^\circ$ in opening angle reconstruction.

199 The detection system consists of fourteen shielded scin- 200 tillators made from Polyvinyl Toluene (PVT) arranged 201 in a ring around the target (see Figs. 2 and 3). At- 202 tached to both ends of each scintillator are 10-cm long, 203 non-scintillating, ultra-violet transmitting, plastic light- 204 guides. A Hamamatsu 580-17 photomultiplier (PMT) 205 tube is fixed to each light-guide using optical glue. In or- 206 der to increase the chance that scintillation light remains 207 inside the scintillator, the scintillators were polished to 208 remove micro-imperfections and were then wrapped in 209 reflective aluminized mylar.

211 Ten out of the fourteen scintillators had dimensions 212 of $76.2 \times 15.2 \times 3.8$ cm 3 . The remaining four, the forward-

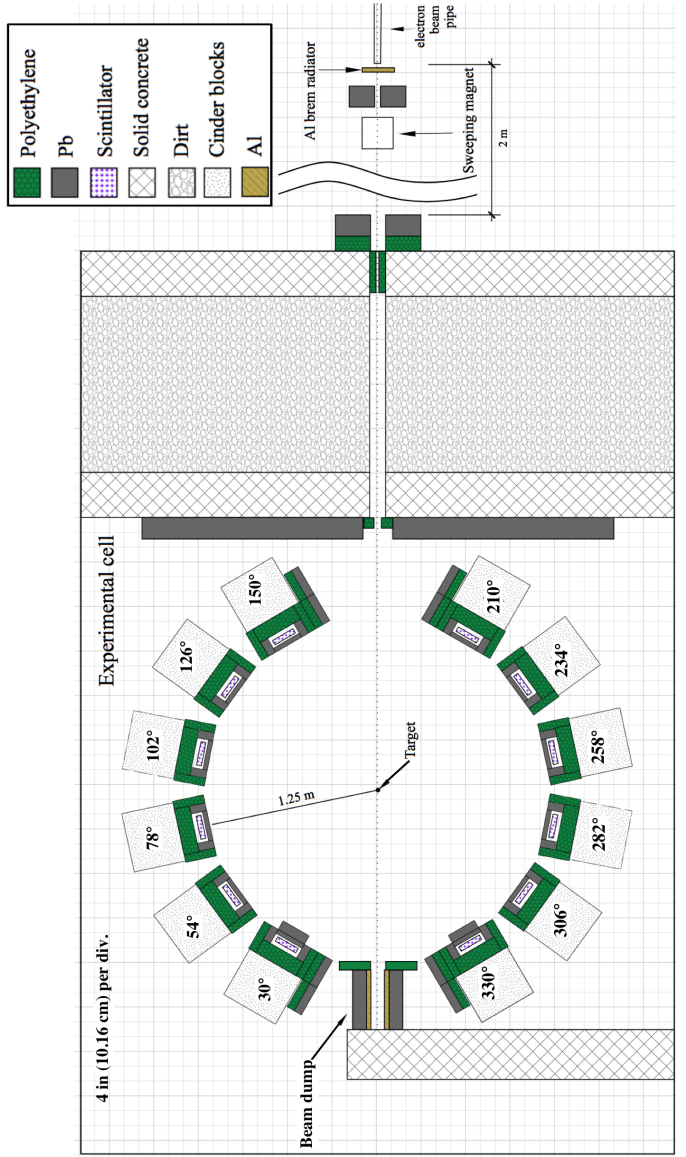


FIG. 2: To-scale, top down diagram of the experimental setup. An electron beam impinges upon a 3.8 cm thick Al radiator, and the resulting bremsstrahlung beam enters the experimental cell from the top of the figure. The supporting structure for each detector has been labeled according to the angle, in degrees, between the center of each detector and direction of the incoming photon beam. The fission target, a $0.05 \times 2 \times 4$ cm 3 ^{238}U cuboid, is rotated slowly about the vertical axis in order to mimic the effect of using a cylindrical target.

213 most detectors located at $\pm 30^\circ$ with respect to the beam, 214 had dimensions of $25.4 \times 15.2 \times 3.8$ cm 3 . These scin- 215 tillators, 1/3 the length of the rest, are the result of the 216 segmentation of two normally sized scintillators in order 217 to address the high photon flux at these locations caused 218 by the forward scattering of photons from the target. 219 Prior to segmentation, a photon was registered in the 220 forward-most detectors at a rate of about 0.9 photons

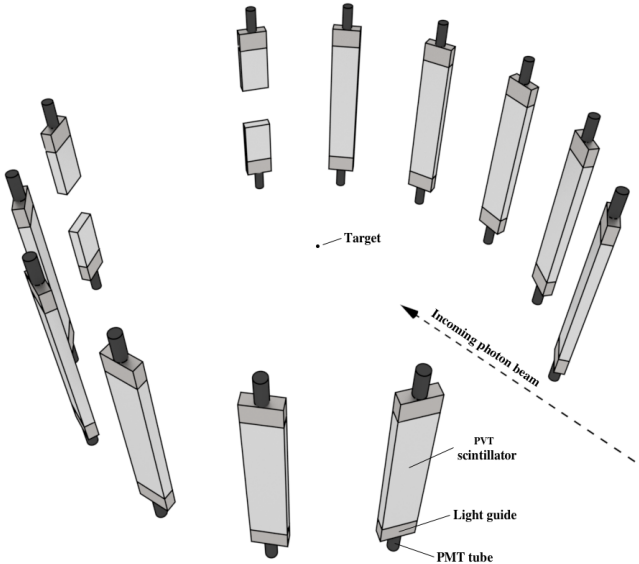


FIG. 3: 3-D rendering of the bare, unshielded scintillators, along with PMTs and light guides. Most of the open space between the scintillators was occupied by shielding, as seen in Fig. 2.

per pulse, and because the electronics were operated in single hit mode (see section II E), this greatly reduced the effective neutron detection efficiency. After segmentation and optimization of shielding, the photon detection rate was about 0.2 photons per pulse in each segmented detector. The segmented detectors also differ from the rest in that they were instrumented with only a single PMT, and therefore provide a comparatively lower precision in energy and position measurements. In order to test for systematic errors that may have resulted from the use of the segmented detectors, opening angle measurements were compared with and without their use, and the differences were well within experimental errors.

The relative efficiencies of the neutron detectors as a function of neutron energy and detector location were calculated by dividing the measured by the known yields of neutrons from the SF of ^{252}Cf . The results are shown in Fig. 4. Note that the effects of the uncertainty in measured neutron energy (see Fig. 10) are folded into this calculation. The analysis techniques described in section IV are designed to eliminate the effects of detector efficiency from the final result.

B. Detector Shielding

The detector shielding, depicted in Fig. 5, was constructed using lead and polyethylene with the aim of reducing detector cross-talk, the detection of photons, and noise. The sides of each scintillator were shielded with 5 cm of lead followed by 5 cm of polyethylene to reduce the chance of neutron cross-talk. Lead was not placed behind the scintillators after an MCNP-POLIMI simulation in-

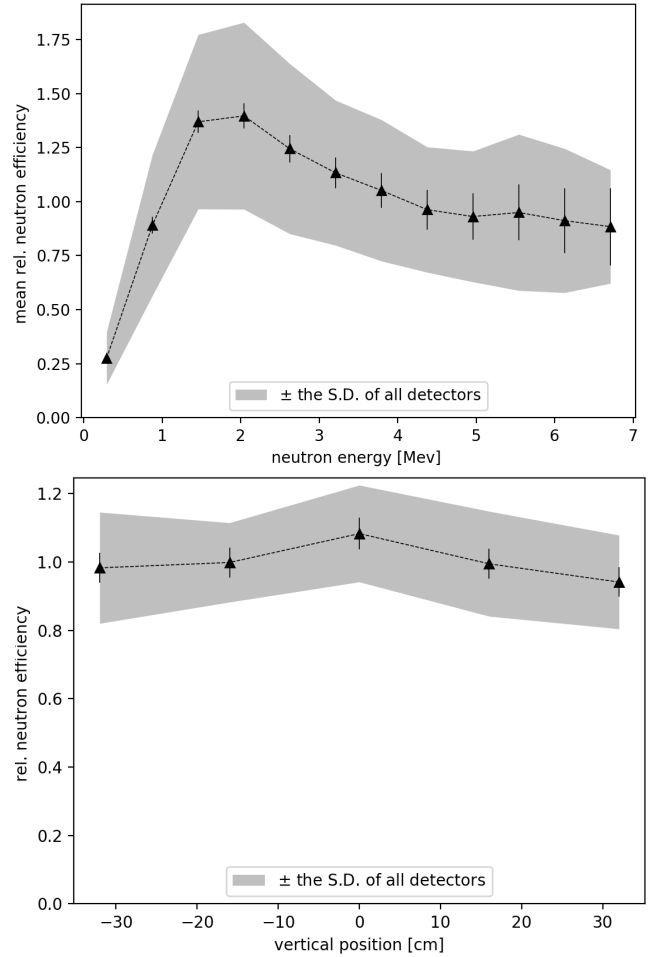


FIG. 4: (top) The mean relative neutron detection efficiency of all detectors as a function of neutron energy is calculated by dividing the measured energy distribution by the known energy distribution of neutrons from the SF of ^{252}Cf . The relative efficiency differs from detector to detector, as demonstrated by the shaded region, which corresponds to the standard deviation of the relative efficiencies of all detectors. The error bars represent the uncertainty in the mean. (bot) Mean relative neutron detection efficiency as a function of the reconstructed position along the detectors longest axis.

dicated that cross-talk would occur at significant rates otherwise. Instead, 10 cm of polyethylene was placed behind the scintillators. For a detailed discussion about the issue of cross-talk, see section V B.

The front face of each detector was subject to the highest photon flux due to the scattering of the bremsstrahlung beam from the target. The detection of a photon renders the given detector unable to detect any subsequent fission neutrons from the same pulse due to the detector recovery time. Lead mitigates this problem by reducing photon flux, but has the side effect of scattering neutrons. If a neutron scatters prior to being detected, the ToF measurement and position reconstruction are incorrect. The extent of measurement errors

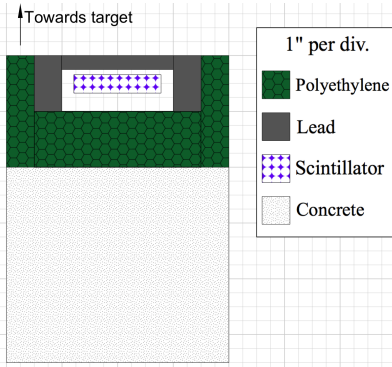


FIG. 5: Detector shielding was designed to reduce the detection of photons, room return, and detector cross-talk.

caused by lead shielding were quantified using an MCNP simulation, and, accordingly, 2.5 cm of lead was placed along the front face of the detectors. This diminished photon detection rates to reasonable levels, and, according to the simulation, leads to a root-mean-square error in opening angle and ToF of 1° and 0.3 ns, respectively, due to neutron elastic scattering.

Because of the particularly high photon flux at the sides of all detectors located directly adjacent to the beam, an additional 2" of lead was placed along the sides of these detectors. For the same reason, an additional 2" of lead was also placed along the front faces of the detectors farthest downstream, located at $\pm 30^\circ$ from the beam line. The differences in shielding design among the detectors can be seen in Fig 2.

C. Bremsstrahlung Photon Beam

In order to ensure that all correlated neutrons produced are due to fission, the bremsstrahlung end-point energy was set to 10.5 MeV, safely below the $(\gamma, 2n)$ threshold of 11.28 MeV for ^{238}U . Aluminum was chosen for the bremsstrahlung radiator because it has a neutron knockout threshold above the energy of the electron beam, which ensured that the radiator would not be a source of fast neutrons with the potential to interfere with the experiment. A sweeping magnet was placed downstream from the bremsstrahlung radiator to remove charged particles from the photon beam. Following the sweeping magnet, the beam traveled through a series of polyethylene and lead collimators on its way into the experimental cell in which the target was located (see Fig. 2). Figure 6 shows the energy distribution of photons that reach the target according to an MCNP simulation that modeled the collimation and production of the bremsstrahlung photons.

The electron beam pulse width was set to 3 ns at a repetition rate of 240 Hz with a 1.1 A peak current. The 3 ns pulse width was small compared to the median neutron ToF of 80 ns, and thus made a small contribution

to the uncertainty in the neutron energy determination.

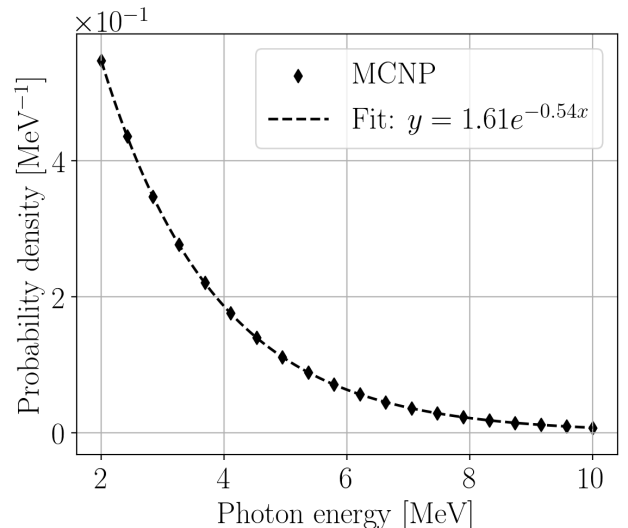
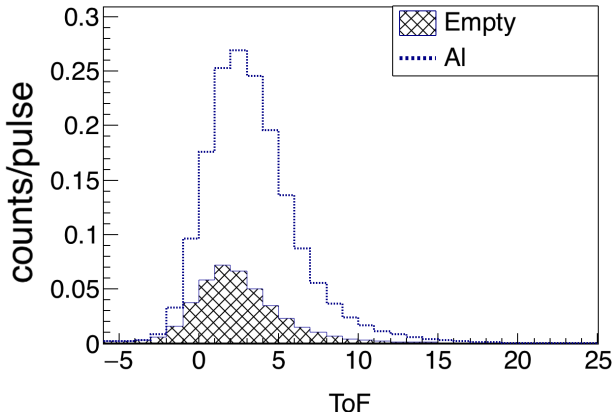


FIG. 6: MCNP simulation of the energy distribution of the bremsstrahlung photons that reach the fission target. Photons with an energy below 2 MeV are excluded.

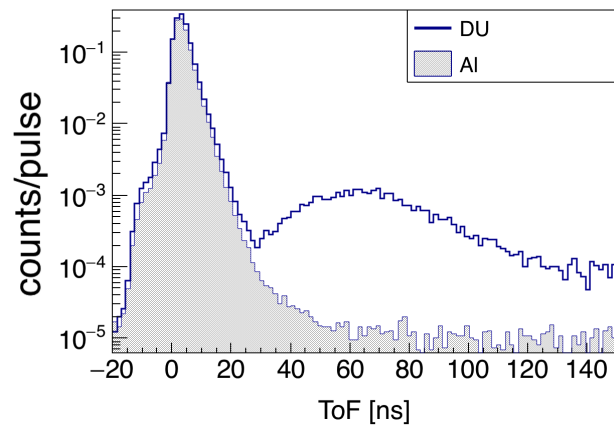
D. DU Target

A depleted uranium (DU) target in the shape of a thin strip with dimensions of $4 \times 2 \times 0.05 \text{ cm}^3$ and a mass of 7.6 g was used as the primary target. ^{238}U was chosen as the fission target because it is an even-even nucleus, and as a consequence, the fission fragments are emitted with a high degree of anisotropy with respect to the photon beam direction [13].

Any target comprised of heavy nuclei has a significant potential to scatter fission neutrons before they exit the target. This is a cause for concern, because neutrons that scatter from heavy nuclei are likely to be deflected at large angles, resulting in the measurement of θ_{nn} 's unconnected to the underlying fission kinematics. As discussed in detail in section V C, an MCNP simulation estimated that 6% of reconstructed θ_{nn} 's are perturbed due to neutron scattering within the ^{238}U target. Moreover, it is more likely that neutrons emitted along the wide, 2 cm, axis of the ^{238}U target undergo a scattering event than neutrons emitted along the thinnest, 0.05 cm, axis. As a result, detectors located collinear to the widest axis of the target would see relatively fewer neutrons due to increased scattering along this axis. This bias is removed by slowly rotating the target about the vertical axis during data acquisition at a rate of one rotation per 8 seconds.



(a)



(b)

FIG. 7: (a) Comparison between the ToF spectrum of a non-neutron producing target made from Al, to the ToF spectrum produced when no target is used. The large increase in events around 4 ns is due to photons that scatter from the Al target. When no target is in place, sources of the peak include the collimator leading into the experimental cell and the beam dump. The photon peak seen here is used to find the timing offsets that make it so $t = 0$ corresponds to the moment of fission. (b) Comparison between the Al and DU targets show a pronounced increase in events between 35 and 130 ns due to the introduction of neutrons.

335

E. Electronics

336 A data acquisition system based on the NIM/VME
 337 standard was used. A schematic of the data acquisition
 338 logic is shown in Figure 8. The PMTs are supplied neg-
 339 ative voltages ranging from 1300 to 1500 V by a LeCroy
 340 1458 high voltage mainframe. Analog signals from the
 341 PMTs were fed into a leading edge discriminator (CAEN
 342 Mod. N841) with input thresholds ranging from 30 mV
 343 to 50 mV. The threshold and supply voltages were deter-
 344 mined individually for each detector to minimize noise,
 345 while simultaneously matching the efficiencies of all the
 346 detectors as closely as possible. Logic signals from the
 347 discriminator were converted to ECL logic and fed into a

348 CAEN model V1290A TDC. The timing of signals from
 349 the PMTs were always measured relative to a signal from
 350 the accelerator provided at the beginning of each pulse.
 351 Even though a multi-hit TDC was used, only the first
 352 signal in each pulse from any given PMT was taken into
 353 account due to concerns over dead-time within the elec-
 354 tronics and signal reflections within the cables. On the
 355 software side, the CODA 2.5 [14] software package de-
 356 veloped by Jefferson Laboratory was used to read out the
 357 data from the TDC and digitally store it for analysis.

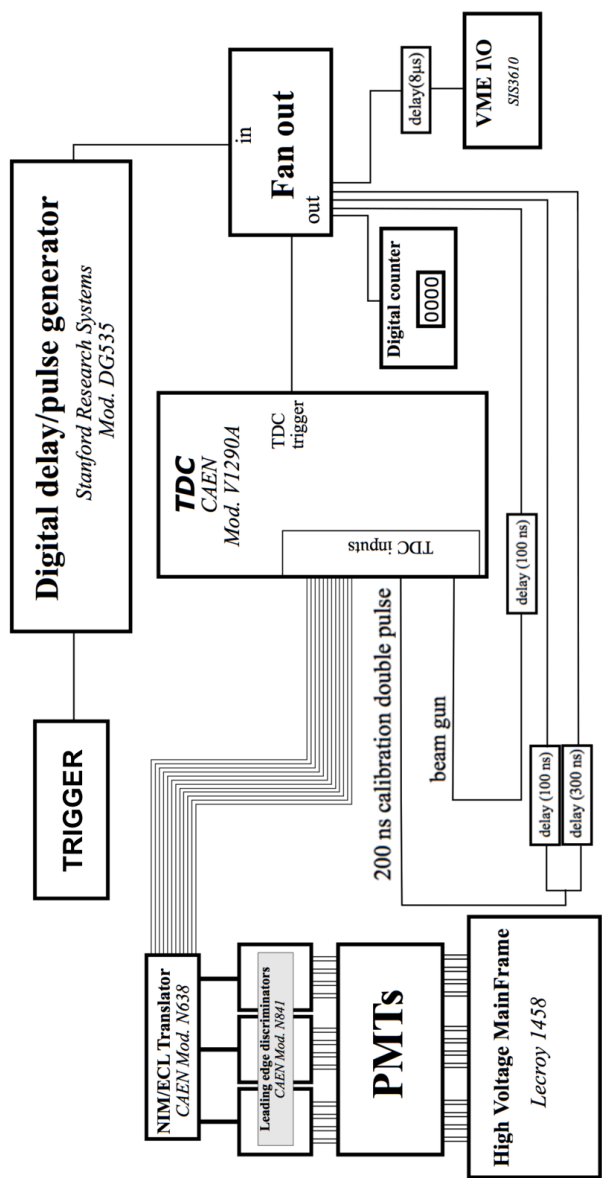


FIG. 8: Wiring diagram of the electronics setup.

358 **III. MEASUREMENT TECHNIQUES**

359 **A. Particle Time of Flight and Energy**
 360 **Determination**

361 The ToF of detected particles is used to distinguish
 362 between neutrons and photons and to determine neutron
 363 energy. A particle's reconstructed position is used to de-
 364 termine direction of motion, which is then used to calcu-
 365 late the opening angle between pairs of detected particles.
 366 Position and ToF are each determined using the timing
 367 of coincident signals from both PMTs of a given detector.

368 The sum of the times required for scintillation light
 369 to travel from the point of scintillation to both PMTs
 370 is equal to the time required for the light to travel the
 371 full length of the scintillator, which is a constant for light
 372 that travels parallel to the length of the scintillator. This
 373 is supported by data, shown in Fig. 9, which were pro-
 374 duced from a series of tests in which a collimated ^{60}Co
 375 source was placed at seven different locations along a
 376 scintillator. One of the two coincident photons emitted
 377 by ^{60}Co reaches the scintillator and the other is detected
 378 by an auxiliary detector serving as the trigger. The pho-
 379 tons incident on the scintillator have a spot size of less
 380 than 1 cm due to source collimation. These events all
 381 have equal transit time, regardless of the ^{60}Co source's
 382 position.

383 In Figure 9(a), it can be seen that the time required
 384 for the scintillation light to propagate along the scintil-
 385 lator has a large effect on the timing of each PMT alone,
 386 however, the average of the times of both PMTs is a con-
 387 stant, unaffected by the location at which the particle
 388 undergoes scintillation. For this reason, taking the aver-
 389 age of signals from two PMTs is advantageous because it
 390 removes the roughly 5 ns timing error that would other-
 391 wise exist due to the time required for scintillation light
 392 to propagate along the scintillator. The requirement that
 393 there be coincident events in both of a detector's PMTs
 394 also aids in reducing noise.

395 During photofission measurements, ToF is calculated
 396 by the following expression:

$$\text{ToF} = t_{\text{mean}}^{\text{PMTs}} - t_{\text{beam}} + C, \quad (1)$$

398 where $t_{\text{mean}}^{\text{PMTs}}$ is the mean of the times of signals from
 399 both PMTs of a scintillator, t_{beam} is the time of a sig-
 400 nal provided by the accelerator at the beginning of each
 401 pulse, and C is a constant timing offset. Any process that
 402 produces a timing delay that does not change from pulse
 403 to pulse contributes to C . For example, the time required
 404 for photons to travel from the bremsstrahlung radiator to
 405 the target, the propagation of signals through the cables
 406 connecting the PMTs, delays in the electronics, etc.

407 The value of C , which may be different for each de-
 408 tector, is determined by comparing the timing spectra
 409 of the gamma flash produced by a non-neutron produc-
 410 ing aluminum target, to that produced when no target is
 411 used. The difference between these two spectra reveals a

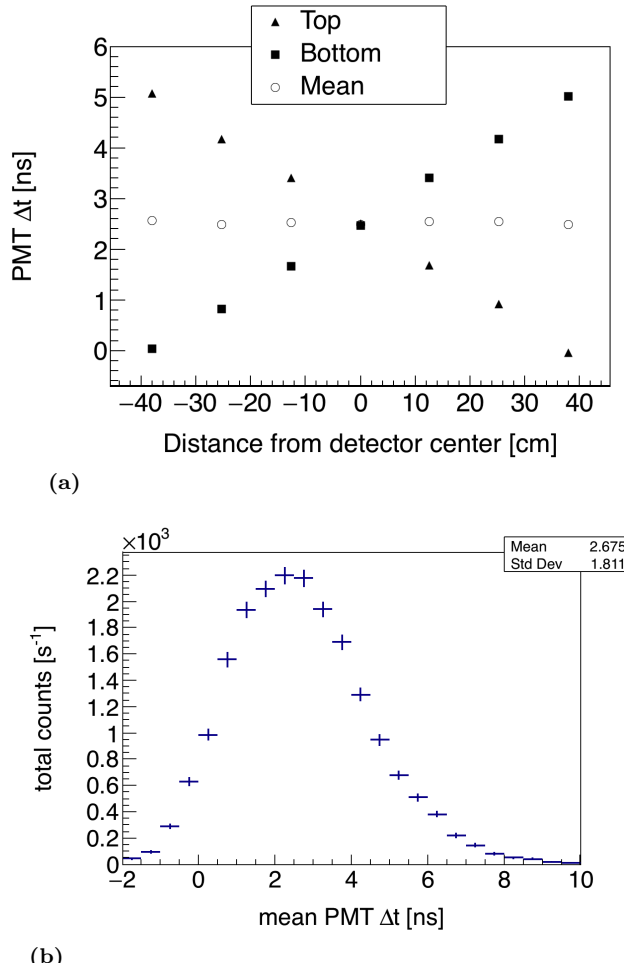
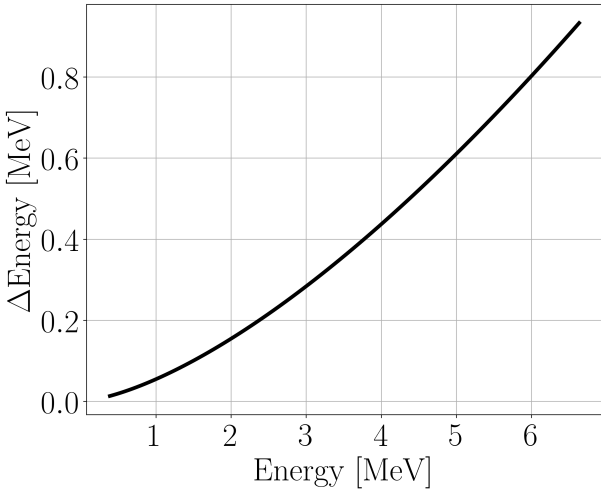


FIG. 9: A collimated ^{60}Co source is used to produce photon events with constant ToF at seven locations along the detector. ^{60}Co produces coincident photons, and one is detected by the scintillator and the other by a separate trigger detector. Δt is the timing of a PMT signal relative to a signal from the trigger detector. In (a), it can be seen that the average between signals from both PMTs does not depend on position. By using the PMT average, there is a reduction in error due to the time required for scintillation light to travel along the scintillator. The uncertainty in ToF measurements is equal to the standard deviation seen in (b), or about ± 2 ns, because all photons from the ^{60}Co source have the same ToF.

412 prominent peak in the ToF spectrum due to photons that
 413 scatter from the aluminum target. These photons must
 414 travel 125 cm to reach the center of any detector and
 415 130 cm to reach the top, for which it takes light 4.2 ns
 416 and 4.3 ns to travel, respectively. The value of C used for
 417 each detector is equal to the value that places the time
 418 corresponding to the peak of the target-induced gamma
 419 flash at 4 ns.

420 The kinetic energy of a detected neutron is determined
 421 straightforwardly from its velocity, which is determined
 422 from its ToF under the assumption that the neutron trav-
 423 eled directly from the target to the detectors unimpeded.



(a)

FIG. 10: Uncertainty in neutron energy measurements as a function of measured neutron energy.

According to a series of MCNP simulations examining the scattering of fission neutrons within detector shielding and the fission target, neutrons predominantly travel to the detectors unimpeded. These simulations are discussed in sections II D and II A.

Figure 10 shows the measurement uncertainty in neutron energy due to error in the ToF determination.

432 B. Particle Position Reconstruction

Each detector is not capable of measuring the position of a detected particle along the axes parallel to its width (15.24 cm) or depth (3.81 cm), which contributes $\pm 3^\circ$ to the total angular uncertainty. The position of a detected particle along the 76.2 cm length of the scintillator is calculated using the timing difference of signals from both of a detector's PMTs. Assuming that scintillation light travels from an initial point, let it be x cm from the center of a scintillator, to both PMTs at a velocity that is constant with respect to the scintillator's length-wise axis, then the difference between the times at which the light will reach each PMT (Δt^{PMTs}) is given by:

$$\begin{aligned} \Delta t^{PMTs} &= t^{PMT_1} - t^{PMT_2} \\ &= \frac{(L/2 + x)n_{\text{eff}}}{c} - \frac{(L/2 - x)n_{\text{eff}}}{c} \\ &= 2x \frac{n_{\text{eff}}}{c}. \end{aligned} \quad (2)$$

Solving for x gives

$$x = \frac{c}{2n_{\text{eff}}} \Delta t^{PMTs}, \quad (3)$$

where t^{PMT_1} and t^{PMT_2} are the times of signals from each of a detector's PMTs relative to the accelerator gun

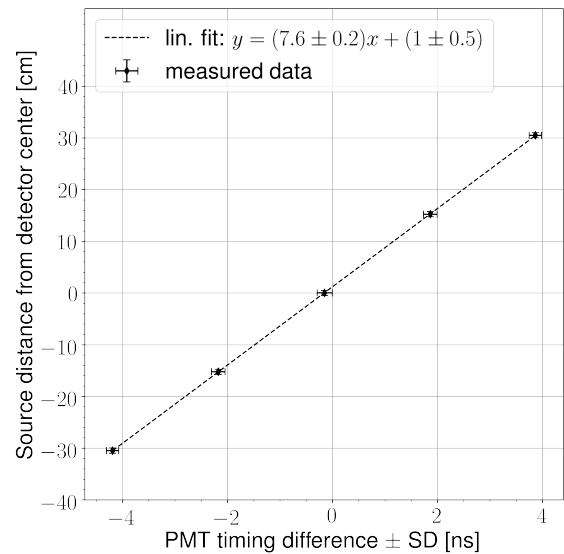


FIG. 11: A collimated ^{60}Co source is used to produce photon events at five different positions along the scintillator. The mean PMT timing difference of events at each position varies linearly with respect to the distance of the ^{60}Co source from the center of the detector. The result of a linear least squares fit to this data is used to calculate the position of detected particles along the length of each scintillator.

pulse, L is the length of the scintillator, c is the speed of light, n_{eff} is the effective index of refraction of the scintillation material. A linear least squares fit between x and Δt^{PMTs} was performed on data gathered using coincident photons emitted by a collimated ^{60}Co source, as described in the previous section. The resulting fit parameters, seen in Fig. 11, are used to find the position of detected particles.

Using the slope of the linear fit in Fig. 11, along with Eq. 3, an effective index of refraction of the scintillation material is calculated to be 2.0. This index of refraction is said to be “effective” because its measurement is sensitive only to the scintillation light’s average speed projected onto the axis parallel to the scintillator’s longest dimension, which is equal to the intrinsic speed of light in the material only if the light is traveling parallel to the scintillator’s length. While the detection of scintillation light by both PMTs favors light paths which are parallel or nearly-parallel to the scintillator’s length, there is some reflection of detected scintillation light from the boundaries of the scintillator. This effect contributes to the ± 9 cm measurement uncertainty in particle position reconstruction. As a result of these effects, the index of refraction measured here is $\sim 25\%$ greater than the true value of the scintillation material.

474

C. Measurements with ^{252}Cf

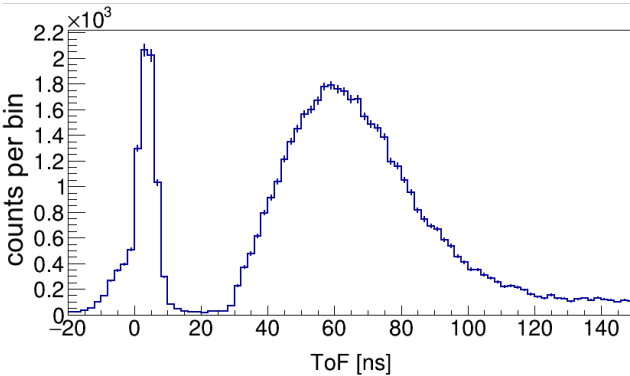


FIG. 12: Measured ToF spectrum from the SF of ^{252}Cf . The sharp peak on the left is due to fission photons, followed by another peak due to fission neutrons.

A ^{252}Cf source was placed at the center of the detection system shown in Fig. 2 in order to measure the n-n opening angle distribution. Several such past measurements have been performed (see Refs. [7–10]), and serve as a means to validate the methods used throughout this study.

The ^{252}Cf source produces a cleaner ToF spectrum than photofission due to the lack of beam related backgrounds (see Fig. 12), and therefore these measurements have a better signal to noise ratio. Also, there is no concern over the detection of accidental neutron coincidences because the fission rate of the ^{252}Cf source was about 3,500 fissions/s, making it highly unlikely that multiple fissions will occur during the electronic acceptance time window of 150 ns. The beginning of the 150 ns neutron acceptance time window was triggered by a 2-fold coincidence, within a 4 ns window, between two separate $10 \times 10 \times 5 \text{ cm}^3$ plastic scintillators, one placed above and the other below the source at a distance of 30 cm. Aside from this difference in the time window triggering mechanism, identical methods were used for both photofission and SF measurements.

IV. ANALYSIS

The efficiency and acceptance of the neutron detection system varies greatly over its opening angle range of 20° to 180° , as illustrated in Fig. 13. This is both due to the neutron detection system's non-spherical symmetry and to varying efficiency as a function of particle position on the detector. In order to give a result that is sensitive to angular correlations, but is highly insensitive to detector efficiencies and experimental drifts in PMT voltage, accelerator current, etc., the angular correlation is determined by dividing a correlated neutron distribution by

an uncorrelated neutron distribution. That is,

$$\text{angular correlation} = \frac{nn_{\text{corr}}(\theta)}{nn_{\text{uncorr}}(\theta)}, \quad (4)$$

where $nn_{\text{corr}}(\theta)$ is the n-n yield after the subtraction of accidental n-n coincidences, and $nn_{\text{uncorr}}(\theta)$ is a convolved distribution of uncorrelated n-n pairs, which is produced by pairing neutron events that occurred during different pulses. The subtraction of accidental n-n coincidences to produce $nn_{\text{corr}}(\theta)$ amounts to a 10% correction, the procedure of which is covered in section IV B. The construction of $nn_{\text{uncorr}}(\theta)$ is described in detail in section IV A.

A. Cancelation of Detector Efficiencies, Drifts, and Geometric Phase Space

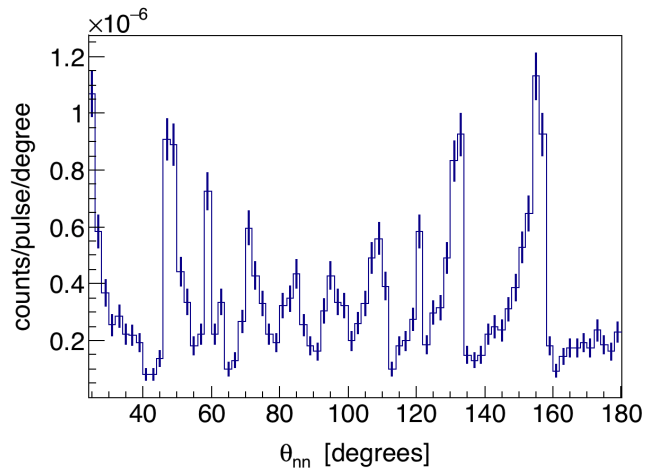


FIG. 13: Raw n-n opening angle yield from the photofission of ^{238}U . This distribution is highly influenced by the detection system's geometric acceptance and efficiency.

The construction of $nn_{\text{uncorr}}(\theta)$ is achieved by pairing detected neutrons that were produced during different accelerator pulses. The same set of pulses used for $nn_{\text{corr}}(\theta)$ is used here, so each of these pulses individually consist of the detection of two coincident neutrons. When constructing $nn_{\text{uncorr}}(\theta)$, it is desirable that the neutrons comprising each uncorrelated n-n pair originated from different pulses that occurred as closely together in time as possible. A smaller time difference between pulses that are paired for this purpose increases the chance that both neutrons were detected under the same experimental conditions amid any drifting of accelerator current, PMT voltages, and varying rates of noise. However, some time difference between the pulses must be allowed so as not to cause insufficient counting statistics. Accordingly, uncorrelated n-n pairs used to construct $nn_{\text{uncorr}}(\theta)$ are formed by neutrons that were detected within 30 minutes or less of each other.

Uncorrelated n-n pairs will have a slightly different joint energy distribution than correlated n-n pairs, which could affect the extent to which the effects of detector efficiency cancel in Eq. 4. This issue is addressed in section V A, where it is shown that these differences have little potential to significantly affect the final result.

Figure 14(a) shows the measured yield distribution of correlated neutrons, $nn_{\text{corr}}(\theta)$, from the photofission of ^{238}U . The structure seen here is reflective of the underlying n-n angular correlations as well as the geometric acceptance and efficiencies of the neutron detectors. Figure 14(b) reveals how a clear picture of n-n angular correlations emerges when taking the ratio between $nn_{\text{corr}}(\theta)$ and $nn_{\text{uncorr}}(\theta)$.

553 B. Subtraction of Accidental Coincidences

The observation of two uncorrelated signals in the neutron ToF range, whether caused by neutrons, photons, or noise, is referred to as an *accidental coincidence*. Accidental coincidences due to noise and photons, which are estimated using a non-neutron producing aluminum target (see Fig. 15), amount to about 3% of all coincidences. Accidental coincidences due to neutrons are minimized by adjusting the accelerator's current so that there are, on average, less than 1.0 fissions per accelerator pulse. Nevertheless, statistical fluctuations in the number of fissions per pulse result in the production of accidental coincident neutrons that originated from different, and therefore, uncorrelated fissions. There are also accidental neutron coincidences caused by the occurrence of multiple (γ, n) reactions in a single pulse. The energy integrated (γ, n) cross-section of ^{238}U , weighted by the bremsstrahlung energy distribution, is about a factor of 5.5 times greater than it is for photofission (see Fig. 16). As a result, the raw n-n coincident yield will contain a significant number of n-n coincidences from multiple (γ, n) reactions in relation to n-n coincidences from fission. The presence of accidental n-n coincidences has the effect of washing out the signal from correlated neutrons.

The raw measurement of n-n yield consists of a mix of correlated and accidental neutron coincidences, that is

$$579 \quad nn_{\text{raw}}(\theta_{nn}) = nn_{\text{corr}}(\theta_{nn}) + nn_{\text{acc}}(\theta_{nn}), \quad (5)$$

where $nn_{\text{raw}}(\theta_{nn})$ and $nn_{\text{acc}}(\theta_{nn})$ are the per-pulse n-n yields as a function of opening angle, θ_{nn} , for all detected n-n pairs, and detected accidental n-n pairs, respectively. As already defined, $nn_{\text{corr}}(\theta_{nn})$ is the per-pulse yield of detected correlated n-n pairs.

Because the n-n coincidences comprising $nn_{\text{acc}}(\theta_{nn})$ consist of two independent detected neutrons, they are governed by the exact same physics and are subject to the exact same experimental conditions as n-n coincidences formed by pairing of single neutrons that were detected during different pulses. Therefore, the opening angle distribution formed by pairing neutrons that

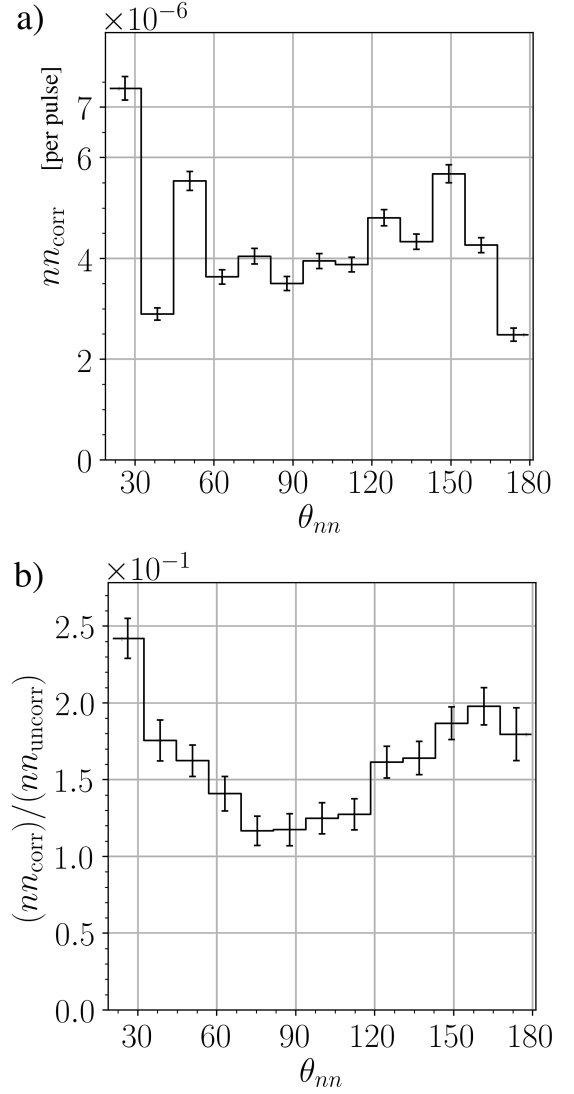


FIG. 14: n-n opening angle distribution from the photofission of ^{238}U before the normalization procedure seen in Eq. 4 (a), and after normalization (b). All measured neutrons have an energy greater than 0.4 MeV.

were detected during different pulses, denoted $nn_{dp}(\theta_{nn})$, is proportional to $nn_{\text{acc}}(\theta_{nn})$. $nn_{dp}(\theta_{nn})$ is constructed from the set of all possible pulse-pairs formed by pulses that occurred within 0.2 seconds of each other. The restriction in time difference is applied in order to increase the chance that pulse pairs together occurred under similar experimental conditions. There are no other restrictions on which pulses can be used in this case. Many pulse-pairs used for the construction of $nn_{dp}(\theta_{nn})$ will contain no detected neutrons.

While $nn_{dp}(\theta_{nn})$ and $nn_{\text{acc}}(\theta_{nn})$ are proportional, $nn_{\text{acc}}(\theta_{nn})$ is not equal to $nn_{dp}(\theta_{nn})$, because there are,

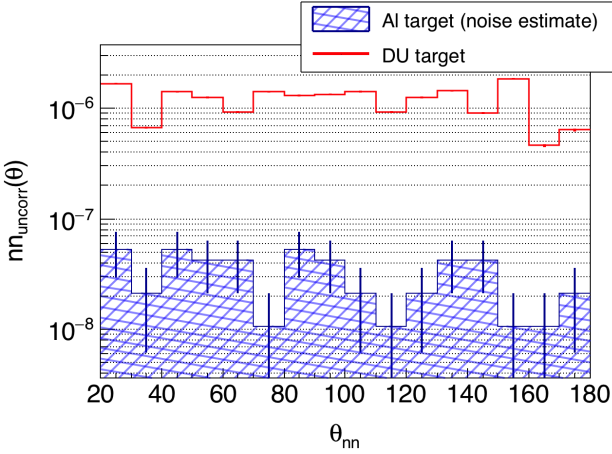


FIG. 15: An Al target was designed have the same thickness, in radiation lengths, as the ^{238}U target, thus serving as an equivalent non-neutron producing target well-suited for noise estimates. The rate of the detection of coincident events in the neutron ToF range while using the Al target was 3% that of the ^{238}U target. Thus, 3% of coincident events used in the determination of n-n angular correlations in ^{238}U can be attributed to noise.

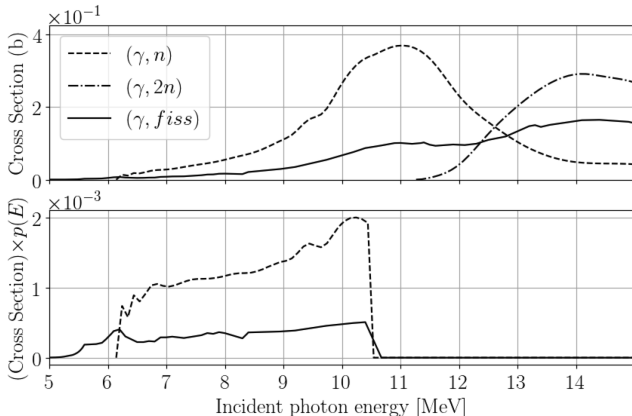


FIG. 16: (top) ENDF cross-sections of (γ, fiss) , direct (γ, n) , and direct $(\gamma, 2\text{n})$. (bottom) Cross-sections weighted by the simulated relative rate of bremsstrahlung photons that reach the target as a function of photon energy. The integrated cross-sections of (γ, n) is 5.5 times greater than for (γ, fiss) . Assuming a $\bar{\nu}$ of 2 neutrons/fission, the bremsstrahlung beam produces about 2.7 times more neutrons via (γ, n) than (γ, fiss) within the target.

on average, more detected neutrons per pulse-pair than per pulse. As the following analysis shows, $nn_{\text{acc}}(\theta_{nn}) = \frac{1}{2}nn_{dp}(\theta_{nn})$, under the condition that $nn_{\text{acc}}(\theta_{nn})$ is normalized to the number of pulses and $nn_{dp}(\theta_{nn})$ to the number of pulse-pairs looked at. When looking at single pulses, the probability of there being a detected uncorrelated n-n pair is denoted by $P_{\text{sp}}^{\text{n-n}}$, and when looking at pulse-pairs, by $P_{\text{dp}}^{\text{n-n}}$. Thus, $P_{\text{sp}}^{\text{n-n}}$ and $P_{\text{dp}}^{\text{n-n}}$ determine the relative rates of $nn_{\text{acc}}(\theta_{nn})$ and $nn_{dp}(\theta_{nn})$, respectively.

The statistics of the detected uncorrelated neu-

trons per pulse is assumed to follow a Poisson distribution, which describes the occurrence of independent random events. Accordingly, the probability of the detection of k uncorrelated neutrons in a given pulse is

$$p(k) = \frac{e^{-\lambda} \lambda^k}{k!}, \quad (6)$$

where λ represents the mean number of uncorrelated detected neutrons per pulse. In principle, λ equals the total number of detected uncorrelated neutrons divided by the total number of pulses. Determination of λ cannot be done in practice, because one would need to know which pairs of detected neutrons are correlated. However, the largest possible value for λ is the total number of detected neutrons divided by the total number of pulses, as this quantity counts all detected neutrons, whether they are correlated or uncorrelated. For this work, that places an upper bound on λ of 5.5×10^{-3} detected uncorrelated neutrons per pulse, which is small enough to truncate all terms beyond the leading term in the following analysis.

Because $P_{\text{sp}}^{\text{n-n}}$ represents the probability of the detection of two uncorrelated neutrons in a single pulse, $P_{\text{sp}}^{\text{n-n}}$ is equal to $p(2)$, as per Eq. 6. Thus,

$$\begin{aligned} P_{\text{sp}}^{\text{n-n}} &= \frac{e^{-\lambda} \lambda^2}{2!} \\ &\approx \frac{\lambda^2}{2} + \mathcal{O}(\lambda^3). \end{aligned} \quad (7)$$

When considering the case of $P_{\text{dp}}^{\text{n-n}}$, recall that, in this case, uncorrelated n-n pairs are formed by examining pulse-pairs. Here, an uncorrelated n-n pair occurs when there is a detected neutron in both pulses. Because all terms beyond the leading term are being truncated, pulse-pairs in which one or both of the pulses comprise two or more detected neutrons do not need to be considered. Thus, $P_{\text{dp}}^{\text{n-n}}$ is equal to the probability of there being exactly one detected neutron in each pulse, which is the square of the probability of there being exactly one detected neutron in a single pulse, namely, $p(1)^2$. Thus, again using Eq. 6,

$$\begin{aligned} P_{\text{dp}}^{\text{n-n}} &= (e^{-\lambda} \lambda)^2 \\ &\approx \lambda^2 + \mathcal{O}(\lambda^3). \end{aligned} \quad (8)$$

Because $P_{\text{dp}}^{\text{n-n}}$ and $P_{\text{sp}}^{\text{n-n}}$ determine the relative rates of $nn_{dp}(\theta_{nn})$ and $nn_{\text{acc}}(\theta_{nn})$, respectively, and because the two distributions have the same shape, from Eq.'s (8) and (7), it follows that

$$nn_{\text{acc}}(\theta_{nn}) = \frac{1}{2}nn_{dp}(\theta_{nn}). \quad (9)$$

Finally, from Eq.'s 9 and 5, the distribution of solely correlated n-n pairs can be recovered from the raw mea-

surement as follows

$$nn_{\text{corr}}(\theta_{nn}) = nn_{\text{raw}}(\theta_{nn}) - \frac{1}{2}nn_{dp}(\theta_{nn}). \quad (10)$$

V. POTENTIAL SOURCES OF ERROR

A. Correlated versus uncorrelated n-n energy distribution

In order to effectively minimize the dependence of the result on detector geometry/efficiency, the numerator and denominator of Eq. 4 must comprise neutron pairs with a similar energy distribution. Note that accidental coincident neutrons from (γ, n) are completely removed from $nn_{\text{corr}}(\theta)$, the numerator in Eq. 4, by the subtraction of accidental coincidences, but are not removed from the denominator, $nn_{\text{uncorr}}(\theta)$. This is the reason for using only pulse-pairs that have two events in each pulse when determining the uncorrelated neutron distribution. Doing so increases the selection of neutrons from fission as opposed to (γ, n) .

When examining differences between the neutron energy distributions in $nn_{\text{corr}}(\theta)$ and $nn_{\text{uncorr}}(\theta)$, it is important to consider how the energies of both neutrons forming n-n pairs vary together, or, in other words, their joint energy distribution. Figure 17 shows the ratio between the rates for correlated and uncorrelated n-n pairs of various binned energies. The effect that these discrepancies in energy distribution have on the final result can be examined by applying a weighting factor to each event in $nn_{\text{uncorr}}(\theta)$ such that a recalculation of the result in Fig. 17 produces a flat curve. A comparison of the angular correlation with and without the application of these weighting factors to uncorrelated n-n events is seen in Fig. 18. The resulting angular correlations are identical to within experimental uncertainties, suggesting that differences in the energy distributions of $nn_{\text{corr}}(\theta)$ and $nn_{\text{uncorr}}(\theta)$ do not significantly affect the present measurement.

B. Detector Cross-talk

Cross-talk occurs when, after a particle is detected once, the same particle, by any means, causes a detection to be registered in a different detector. For example, upon detection, a particle may undergo elastic scattering and then travel into another detector where it is detected again, or, it may produce secondary particles that are detected. The two coincident detections of a cross-talk event are causally correlated, and thus they have the potential to contaminate the signal from correlated fission neutrons. If both detections occur during the ToF range typical for fission neutrons, then the cross-talk event cannot be distinguished from the detection of two correlated neutrons.

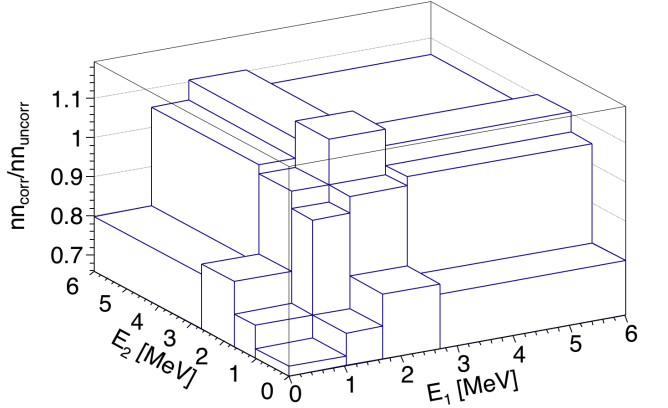


FIG. 17: The z-axis represents the ratio between the correlated and uncorrelated rates of binned n-n energies. The energy bins are chosen such that each contains an equal number of events, or 1/16th of the total events.

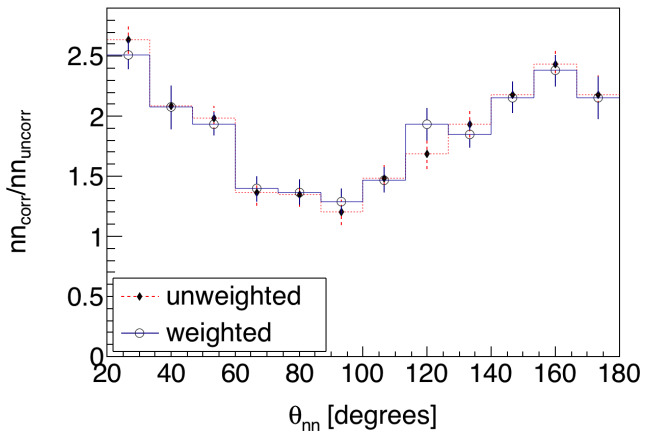


FIG. 18: Each uncorrelated n-n event can be weighted such that the weighted histograms of the joint n-n energy distributions of correlated and uncorrelated n-n pairs are equal. Comparison of the calculated angular correlation results, with and without such weighting factors applied to all uncorrelated n-n events, illustrates that any effects due to the discrepancies in the joint energy distributions of correlated and uncorrelated n-n pairs are negligible.

Recent works that measured the n-n angular correlations in the spontaneous fission of ^{252}Cf and ^{240}Pu [8, 12] addressed this effect by using an MCNP-PoLiMi simulation to estimate and then subtract cross-talk from their measurements. In this work, the issue of cross-talk is approached differently by employing the use of detector shielding aimed at reducing cross-talk to a negligible rate. By using shielding to reduce cross-talk, this measurement is less dependent on the details of the models used by MCNP-PoLiMi to simulate neutron transport and detection. MCNP-PoLiMi simulations are used in this work only to verify that the effect of cross-talk is negligible.

The scintillators used here are much larger than those used in similar works, such as in Refs. [8, 12], allowing them to be placed much farther from the fission source

718 without causing a detrimental loss in coincidence rates.
 719 An increase in the distance between the detectors and the
 720 fission source makes this measurement less subject to to
 721 angular uncertainty, which depends directly on the un-
 722 certainty in the position of a detected particle due to, for
 723 example, the scattering of neutrons from detector shield-
 724 ing. For this reason, larger amounts of shielding can be
 725 used without concern of introducing large errors.

726 Furthermore, the geometry of the neutron detection
 727 system makes it kinematically impossible for a neutron
 728 to undergo a single scattering event with a proton in one
 729 detector, which is the basis for scintillation, and then
 730 travel directly into another detector with enough kinetic
 731 energy to be detected a second time. For this reason,
 732 upon being detected, a neutron must scatter from one or
 733 more intermediate nuclei, such as lead or carbon, in or-
 734 der for it to reach another detector with enough energy
 735 to be detected again. This fact follows from the con-
 736 servation of energy and momentum. In order to support
 737 the claim that the design of the neutron detection system
 738 reduced cross-talk to negligible rates, a detailed MCNP-
 739 PoliMi [15] simulation was performed in which a built-in
 740 ^{252}Cf source is positioned at the center of a model of the
 741 neutron detection system.

742 1. Simulation of Detector Cross-talk

743 The cross-talk simulation included all scintillators,
 744 shielding, detector supporting structures, and the con-
 745 crete walls surrounding the experimental cell. MCNP-
 746 PoliMi's built-in ^{252}Cf spontaneous fission source was
 747 used, which emits neutrons with the correct corre-
 748 lations and multiplicities according to previous measure-
 749 ments. Detector response was modeled using a program
 750 included with the MCNP-PoliMi distribution called MP-
 751 Post [16]. The model is based on the MeV electron equiv-
 752 alent (MeVee) light output produced by particles as they
 753 undergo collisions with carbon and hydrogen within or-
 754 ganic plastic scintillators. A minimum deposited energy
 755 of 0.4 MeV (equivalent to 0.05 MeVee for neutrons) was
 756 assumed for detectable particles, which was chosen be-
 757 cause the neutron detection system exhibited a sharp de-
 758 cline in detection efficiency for neutrons below 0.4 MeV.
 759 For neutron collisions with hydrogen, the light output
 760 in MeVee, denoted L , is calculated by the following em-
 761 pirically derived formula [16]

$$L = 0.0364\Delta E_n^2 + 0.125\Delta E_n,$$

762 where ΔE_n is equal to the loss in the kinetic energy of the
 763 neutron due to the collision. Neutron interactions with
 764 carbon are assumed to generate a small light output of

$$L = 0.02\Delta E_n.$$

765 As seen in Fig. 19, this model of the detection process
 766 produces a ToF spectrum for the SF of ^{252}Cf that shows
 767 good agreement with the measurement for neutrons with

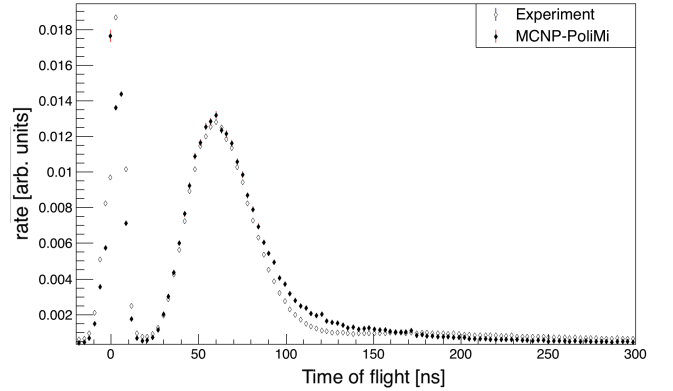


FIG. 19: Measured versus simulated ToF spectrum from the SF of ^{252}Cf . The simulation used the detector response model outlined in ref [16]. The simulated and measured curves are normalized in order to facilitate comparison.

768 a ToF less than 100 ns and fair agreement for neutrons
 769 with a ToF greater than 100 ns.

770 Figure 20 shows the distribution of cross-talk events
 771 and true n-n coincidences as a function of reconstructed
 772 opening angle. It is worth noting that, according to this
 773 simulation, the effect of cross-talk is not only small, but is
 774 also distributed over a wide range of angles rather than
 775 being concentrated around 0 degrees as one might ex-
 776 pect. Angles greater than 125 degrees are not shown
 777 in Fig. 20 because cross-talk events at large angles can
 778 be readily identified in analysis due to the large amount
 779 of time required for a neutron to travel these distances.
 780 The simulation was initially performed with 5 cm of lead
 781 shielding placed behind the scintillators, and the num-
 782 ber of cross-talk events accounted for 11% of the total
 783 coincident neutron events. This value fell to 3% when
 784 polyethylene was used instead of lead, motivating the
 785 placement of 10 cm of polyethylene behind the detectors
 786 instead of lead.

789 C. Neutron Scattering within the Target

790 A potential source of error in opening angle measure-
 791 ments is the scattering of emitted neutrons as they tra-
 792 verse the fission target. This is a cause for concern be-
 793 cause when neutrons scatter from heavy nuclides such
 794 as ^{238}U , they are likely to be deflected at large angles
 795 resulting in n-n opening angles that do not reflect the
 796 true underlying fission kinematics. The effect that this
 797 has on this work is assessed by MCNP simulations. In
 798 summary, for 6% of n-n pairs, at least one neutron out
 799 of the two scatters before exiting the target, according to
 800 the simulation. This effect does not have a large influ-
 801 ence on the measured θ_{nn} distribution according to the
 802 simulation data shown in Fig. 21.

803 The rate of elastic scattering is affected by the size
 804 and shape of the target. A thin strip is the ideal target
 805 shape regarding the rate of neutron elastic scattering per

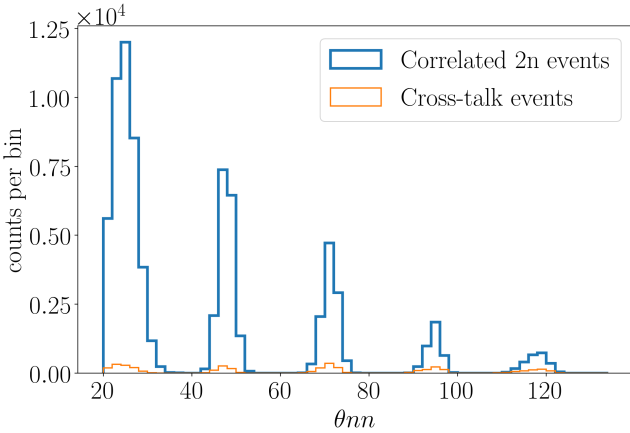


FIG. 20: MCNP-PoLiMi simulation of the number of cross-talk events versus correlated n-n events as a function of reconstructed opening angle. Cross-talk accounted for 3% of total events. Simulated cross-talk events do not occur primarily at small angles, but are instead spread out over a wide range of angles. Any cross-talk occurring at angles larger than 125° will be removed from the experimental data by the cuts applied to neutron ToF.

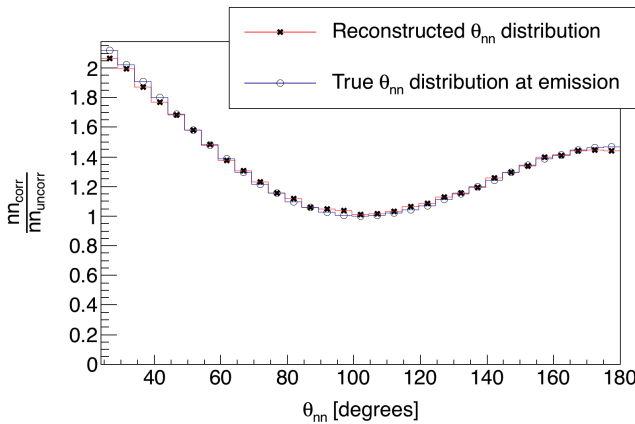


FIG. 21: MCNP-PoLiMi simulation of correlated ^{252}Cf neutrons sampled uniformly throughout a $0.05 \times 2 \times 4 \text{ cm}^3$ U-238 target. The slight difference between the curves is due solely to the elastic scattering of neutrons within the target, since detector physics was not simulated. In the reconstructed θ_{nn} distribution (\star), only neutrons which enter a physical volume at which a detector was located during the experiment are counted. The true θ_{nn} distribution at the moment of emission is also plotted (\circ).

806 unit of total target volume. See Fig. 22 for the simulated
807 elastic scattering rates for both thin strip and cylindrical
808 shaped targets. The simulation indicated that the rate of
809 elastic scattering in cylindrical targets is about a factor
810 of two times greater than in thin strip targets with the
811 same volume.

812 The target's dimensions are small enough that the
813 rate of photon absorption, and thus photo-neutron pro-
814 duction, is virtually uniform throughout the entire tar-
815 get volume. An MCNP-PoLiMi simulation was used
816

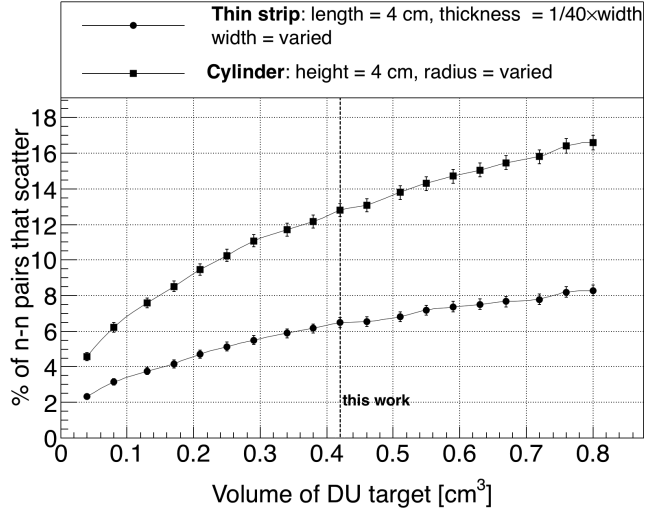


FIG. 22: Result of an MCNP simulation in which n-n pairs, with energies sampled from a typical watt fission spectrum, were generated uniformly throughout the volume of DU targets. The y-axis is the rate of opening angle contamination due to the scattering of, within the DU target in which they were produced, either one or both of a pair of neutrons. The lack of symmetry of a thin strip target can be removed by slowly rotating the target around the vertical axis during data acquisition, making it the optimal target geometry for the minimization of the rate of neutron scattering. The target used in this work had a length of 4 cm, a width of 2 cm, and a thickness of 0.05 cm.

818 to generate ^{252}Cf spontaneous fission events uniformly
819 throughout the target. The SF of ^{252}Cf is used instead
820 of the photofission of ^{238}U because of the current lack
821 of photofission models, however, the underlying fission
822 kinematics are, broadly speaking, the same for the SF of
823 ^{252}Cf and the photofission of ^{238}U . Thus, the two pro-
824 cesses have similar n-n correlations.

825 Section VI B discusses the observation of an unex-
826 pected drop in correlation around 180° in our photofis-
827 sion of ^{238}U measurement, as seen in Figs. 23 and 24.
828 This motivated a second simulation regarding elastic
829 scattering which examined whether this decrease in the
830 correlation around 180° opening angles reflects the un-
831 derlying physics of the fission process. In particular, note
832 that throughout these measurements, the target was con-
833 tinuously rotated once per 8 seconds. This means that for
834 the determination of the uncorrelated opening angle dis-
835 tribution, the trajectories of the two neutrons were taken
836 from two different pulses in which the target was at a dif-
837 ferent orientation for each of them. Additionally, each of
838 the neutrons likely originated from different regions of the
839 target volume. On the other hand, for the same-pulse,
840 correlated neutron measurement, the target was in the
841 same orientation and the two neutrons were generated
842 at the same position in the target. For these reasons,
843 the rates of neutron scattering within the target are not
844 necessarily equal for the same-pulse and different-pulse
845 cases. As such, we investigated whether these differences

846 could cause this apparent decrease in the opening angle
847 distribution near 180° .

848 Using the correlated ^{252}Cf SF source built-in to
849 MCNP-PoLiMi, the opening angle distribution of neu-
850 trons at the moment of emission, labeled *true* in Fig. 21,
851 were compared to that of the neutrons after they have es-
852 caped the target, labeled *reconstructed* in Fig. 21. The lo-
853 cation of fission events were sampled uniformly through-
854 out the target's volume. The analysis employs the same
855 technique outlined in section IV A, in which a correlated
856 neutron distribution is divided by an uncorrelated neu-
857 tron distribution. The correlated neutron distribution is
858 formed by pairing neutrons emitted during the same fis-
859 sion, and the uncorrelated distribution by the pairing of
860 neutrons emitted during different fissions. In order to
861 account for the effect of a rotating target on the trajec-
862 tories of neutrons from different-pulses, the coordinate
863 system was rotated about the vertical axis accordingly
864 for different fission events. The result from this simu-
865 lation suggests that the rotating $0.05 \times 2 \times 4 \text{ cm}^3$ U-238
866 target does not, due to neutron scattering, result in a
867 measurable departure from the true n-n opening angle
868 distribution.

869

VI. RESULTS

870 The n-n opening angle correlation is calculated using
871 the methods outlined in Sec. IV, in which a correlated
872 neutron yield is divided by an uncorrelated yield. The
873 results are compared with output from FREYA [17] (Fis-
874 sion Reaction Event Yield Algorithm), which was de-
875 veloped by the collaborative efforts of researchers from
876 Lawrence Berkeley National Laboratory, Lawrence Liv-
877 ermore National Laboratory, Los Alamos National Labo-
878 ratory, and University of Michigan Nuclear Engineering,
879 and has been included in MCNP beginning with version
880 6.2.

881 The most recent release of FREYA (version 2.0.3)
882 does not model photofission directly, but instead uses
883 a neutron-induced fission model as an *ad hoc* photofis-
884 sion model [18]. Modeling photofission in this manner is
885 a crude approximation, unbacked by experimental verifi-
886 cation. Nonetheless, due to the current lack of accepted
887 photofission models, the approximate model included in
888 FREYA version 2.0.3 is compared with the results of the
889 present work.

890 For a given nucleus with Z protons and A total nucle-
891 ons, the code selects the neutron-induced fission model
892 for a Z(A-1) nucleus, and chooses an incident neutron
893 energy such that the compound ZA nucleus will have,
894 relative to ZA's ground state, an excitation energy that
895 is equal to the energy of the would-be incident photon.

896 When using FREYA to model photofission in this
897 work, all model parameters, such as level density and
898 partition parameters, were set to their default values for
899 neutron-induced fission. FREYA was configured to use
900 the fission fragment mass distribution, $Y(A)$, and the

901 average total kinetic energy, $\langle \text{TKE} \rangle(A)$, from the ^{238}U
902 photofission measurements described in Ref. [19].

903 A. n-n angular correlation versus neutron energy

904 The measured θ_{nn} distribution from the photofission of
905 ^{238}U and the SF of ^{252}Cf are presented with the following
906 two different types of cuts applied to the energies of neu-
907 trons in coincidence: in Figs. 23 (^{238}U) and 25 (^{252}Cf), a
908 minimum energy threshold is applied to both neutrons,
909 and in Figs. 24 (^{238}U) and 26 (^{252}Cf), the energy of both
910 neutrons are required to fall within a specified range

911 In each of Figs. 23 through 26, the data are reported
912 using two representations: the classic histogram and the
913 kernel density estimate (KDE). When using a histogram
914 to estimate a continuous distribution from the relatively
915 small number of data points obtained in this work, one
916 faces the following dilemma: small bin-widths lead to
917 large uncertainties that are dependent on the chosen bin-
918 width, while large bin-widths obscure potentially useful
919 information. This problem is mitigated by the use of a
920 KDE. A KDE is a method for estimating a continuous
921 probability distribution from a finite set of sampled data
922 points. The kernel was chosen to be the measurement
923 errors in opening angle as determined by a study using
924 coincident photons from a ^{60}Co source, which was placed
925 at different locations along a detector. The measurement
926 errors in θ_{nn} are well-described by a gaussian with a stan-
927 dard deviation of 6° . Mathematical details of the KDE
928 method used in this work are outlined in Ref. [20]. The
929 error bands seen in Figs. 23 through 26 correspond to
930 68% confidence intervals.

931 Plotted alongside each measurement is the result of
932 a FREYA simulation. For the measurement of ^{238}U
933 photofission, there were a total of 2,952 n-n coincident
934 events after the subtraction of accidentals, and for the
935 SF of ^{252}Cf , there were 21,882.

936 B. Considering θ_{abs}

937 While the results reported in the previous section are
938 consistent with the effect of the kinematic focusing of the
939 neutrons due to the recoil of the fission fragments, the
940 data for U-238 show a statistically significant decrease
941 in the n-n opening angle correlation in the region from
942 about 165° to 180° , which can be seen in Figs. 14 and
943 28, as well as in Figs. 23 and 24. The effect is particularly
944 strong for the neutron energy cuts being applied in the
945 upper right plots of both Figs. 23 and 24. A comparison
946 of the observed decrease after 160 degrees with the null
947 hypothesis that the true distribution remains constant af-
948 ter 160 degrees yields a p-value of 0.01. This indicates a
949 1% probability of obtaining data as compatible with the
950 above hypothesis as the data we observed. This is a fea-
951 ture which does not seem to universally appear in either
952 neutron-induced or spontaneous fission. A similar but

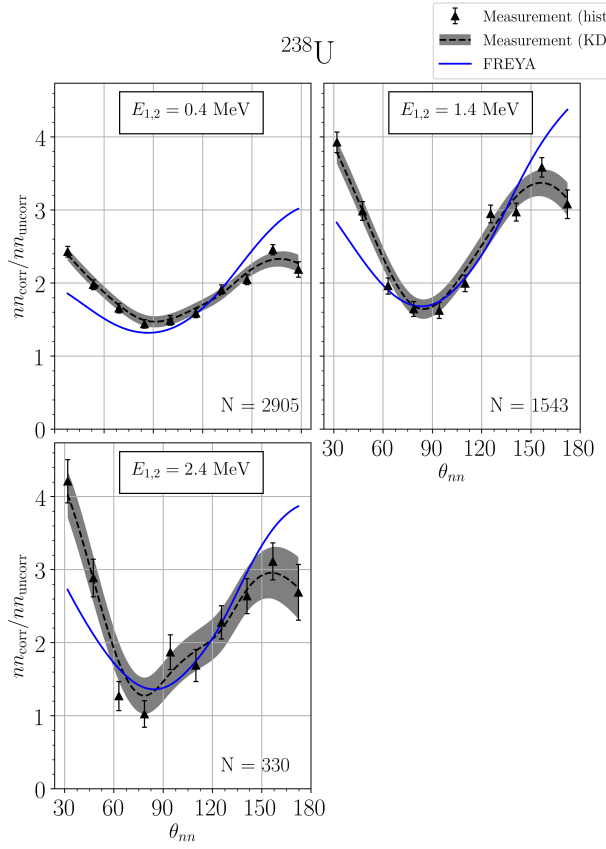


FIG. 23: θ_{nn} distribution with minimum neutron energy cuts applied. The number of events contributing to each plot, n , is shown. Note that the bottom plots of this figure and Fig. 24 are identical.

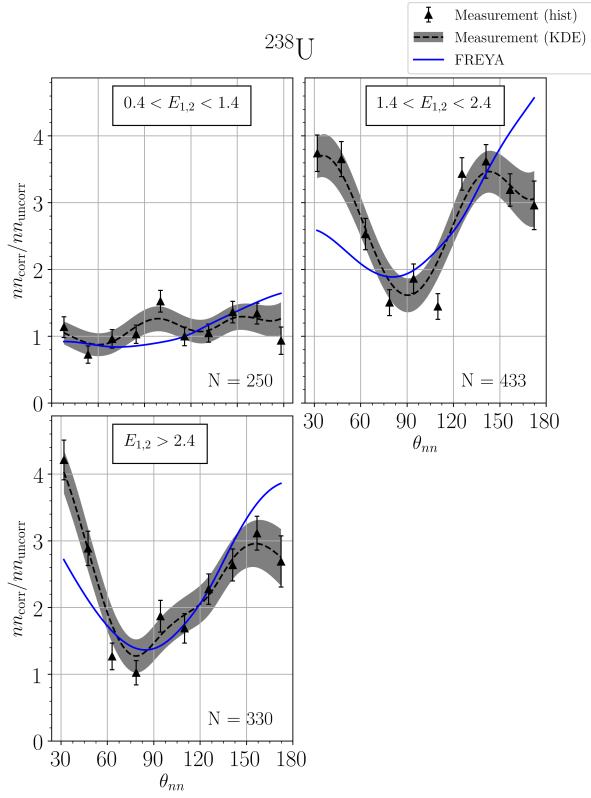


FIG. 24: θ_{nn} distribution with cuts requiring that the energy of both coincident neutrons be within the specified range. The number of events contributing to each plot, n , is shown. Note that the bottom plots of this figure and Fig. 23 are identical.

less pronounced effect appears in the results reported in Ref. [11] for the thermal neutron-induced fission of ^{233}U and ^{235}U , but not for the spontaneous fission of ^{252}Cf or the neutron-induced fission of ^{239}Pu . The prominence of this effect observed in the present work may be a characteristic feature of the photofission of the even-even ^{238}U nucleus.

As previously discussed in section IC, photofission differs from spontaneous and neutron induced fission in that the fission fragments for the photon-induced reaction exhibit an asymmetry in their angle of emission, with the most likely orientation of the fission axis lying perpendicular to the direction of the incident photon. With this in mind, the following series of angular cuts were made on the data. Figure 27 shows the distributions of absolute opening angles of the n-n events for three different cuts on the value of the n-n opening angle. For n-n opening angles between 120° and 160° , there is an increased preponderance of both neutrons being emitted around 90° , consistent with the interpretation of kinematic focusing of neutrons coming from fission fragments which are themselves being emitted preferentially at 90° . However, in the opening angle region where the n-n correla-

tion is reduced, from about 160° to 180° , this feature is less prominent.

Furthermore, if one plots the opening angle distributions for the case in which at least one neutron is emitted perpendicular to the incident photon versus the case in which neither neutron is emitted perpendicular to the incident photon (Fig. 28), one sees distinct differences.

The fact that there are overall differences is not surprising, because in one case (Fig. 28 solid line) at least one neutron preferentially receives a kinematic boost from a fission fragment and in the other case (Fig. 28 dotted line) neither neutron does. However, the fact that the n-n correlation is reduced at 180° in opening angle when at least one of the neutrons is emitted along the preferred fission axis is unexpected. This is a feature which does not seem to appear in most previous measurements of either neutron-induced or spontaneous fission, as well as our present measurement on spontaneous fission. The attribution of this effect to the geometric coverage of the neutron detection system or to neutron elastic scattering within the target was ruled out using simulations, as discussed in section VC.

These data are consistent with two possible explanations relating to the unique feature of the asymmetric an-

^{252}Cf (SF)

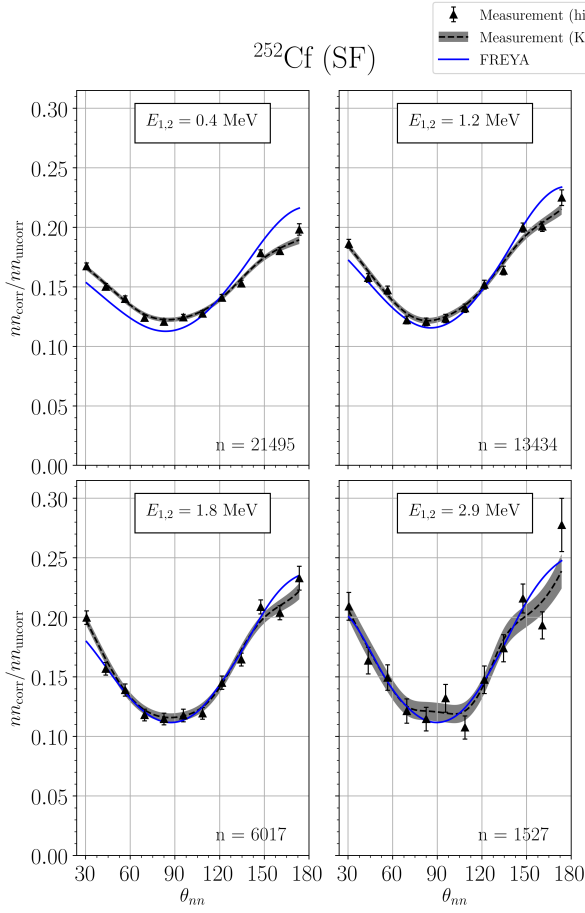


FIG. 25: θ_{nn} distribution with minimum neutron energy cuts applied. The number of events contributing to each plot, n , is shown. Note that the lower right plots of this figure and Fig. 26 are identical.

gular emission of fission fragments in photofission. First, the neutrons may indeed be emitted isotropically in the rest frame of the fission fragment, but one fragment essentially shadows the neutrons emitted from the other fragment, either through absorption or scattering. Second, that there is, due to unknown reasons, a decrease in neutron emission along the fission axis. If it is the former case, then this effect has the potential to shed light on the time dependence of neutron emission, since shadowing would likely depend on the fission fragment separation. A definitive interpretation of this decreased n-n correlation for large opening angles in photo-fission requires further study.

1013

VII. CONCLUDING REMARKS

1014 Neutron-neutron angular correlations in the photofission of ^{238}U were measured using 10.5 MeV end-point
1015 bremsstrahlung photons produced via a low duty factor,

^{252}Cf (SF)

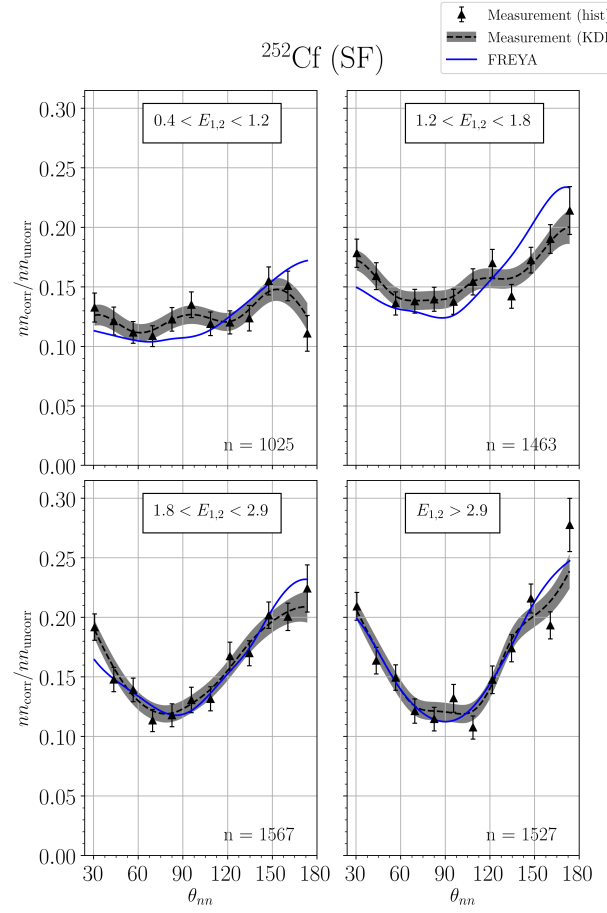


FIG. 26: θ_{nn} distribution with cuts requiring that the energy of both coincident neutrons be within the specified range. The number of events contributing to each plot, n , is shown. Note that the lower right plots of this figure and Fig. 25 are identical.

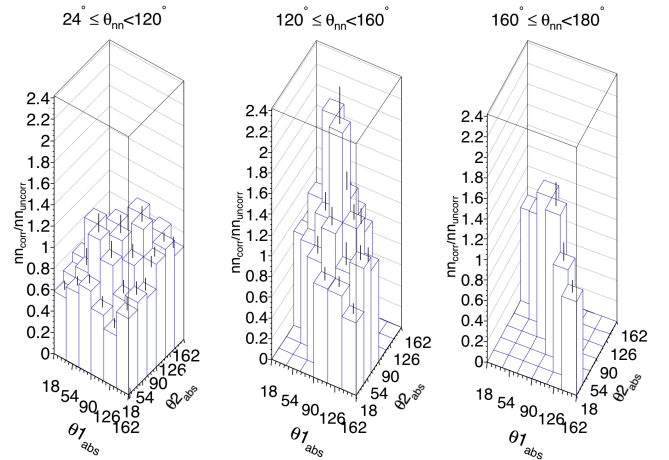


FIG. 27: Visualization of the correlation between the angles of each neutron with respect to the incident photon beam, denoted by $\theta_{1,abs}$ and $\theta_{2,abs}$. Empty bins exist because of intrinsic geometrical phase-space. Data taken from measurements of ^{238}U photofission.

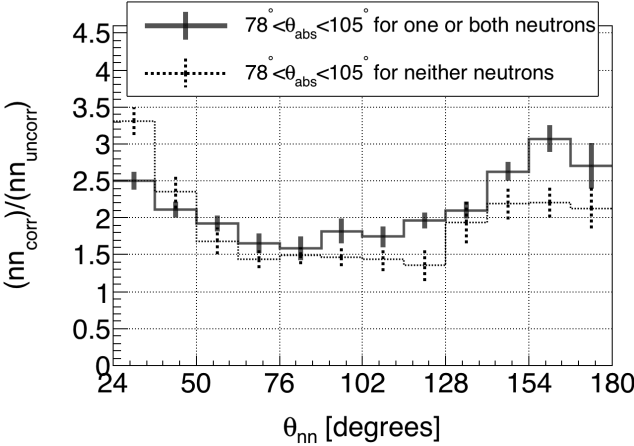


FIG. 28: Requiring that at least one of the coincident neutrons be emitted nearly perpendicular to the photon beam (solid line) produces an opening angle distribution that is different from that produced when it is required that both neutrons are emitted nearly parallel to the photon beam (dotted line). Data taken from measurements of ^{238}U photofission.

pulsed linear electron accelerator. The measured angular correlations reflect the underlying back-to-back nature of the fission fragments. The method of analysis used a single set of experimental data to produce an opening angle distribution of correlated and uncorrelated neutron pairs. A ratio is taken between these two sets to provide a self-contained result of angular correlations, in that the result is independent of neutron detector efficiencies. Neutron-neutron angular correlation measurements were also made using neutrons from the spontaneous fission of ^{252}Cf and show good agreement with previous measurements.

Measured n-n opening angle distributions from the photofission of ^{238}U are in great disagreement with the ad

hoc photofission model included in FREYA version 2.0.3. This is expected, because the model is only a crude approximation which uses a neutron-induced model to approximate photofission. The present measurement will be useful for fine-tuning photofission models included in future releases of FREYA.

In addition, we report for the first time a pronounced anomaly in the n-n angular distributions from photofission, in which the rate of neutron emission at opening angles near 180° is diminished, resulting in a local maximum at about 160° instead of the expected 180° . We offer two possible explanations for this effect. First, the neutrons may indeed be emitted isotropically in the rest frame of the fission fragment, but one fragment essentially shadows the neutrons emitted from the other fragment, either through absorption or scattering. Second, that there is, due to unknown reasons, a decrease in neutron emission along the fission axis. While these measurements do not provide a definitive interpretation of this decreased n-n correlation for large opening angles in photofission, further study may have the potential to shed light on the time evolution of neutron emission in photofission.

These first measurements of n-n correlations in photofission may provide the impetus for future modeling of the fundamental physics of fission.

VIII. ACKNOWLEDGMENTS

This work has been supported by the National Nuclear Security Administration, grant DE-NA002488. We wish to thank the staff of the Idaho Accelerator Center for their assistance in this work. We also wish to acknowledge early contributions to this work by our friend and

colleague the late David V. Jordan of the Pacific Northwest National Laboratory.

-
- [1] J. T. Caldwell, E. J. Dowdy, R. A. Alvarez, B. L. Berman, and P. Meyer. Experimental determination of photofission neutron multiplicities for ^{235}U , ^{236}U , ^{238}U , and ^{232}Th using monoenergetic photons. *Nuclear Science and Engineering*, 73(2):153–163, 1980.
- [2] G. A. Petrov. Current status of the search for scission neutrons in fission and estimation of their main characteristics. *AIP Conference Proceedings*, 798(1):205–212, 2005.
- [3] Harry R. Bowman, Stanley G. Thompson, J. C. D. Milton, and Wladyslaw J. Swiatecki. Velocity and angular distributions of prompt neutrons from spontaneous fission of Cf^{252} . *Phys. Rev.*, 126:2120–2136, Jun 1962.
- [4] C. Budtz-Jørgensen and H.-H. Knitter. Simultaneous investigation of fission fragments and neutrons in ^{252}Cf (SF). *Nuclear Physics A*, 490(2):307 – 328, 1988.
- [5] P. Talou, R. Vogt, J. Randrup, M. E. Rising, S. A. Pozzi, J. Verbeke, M. T. Andrews, S. D. Clarke, P. Jaffke, M. Jandel, T. Kawano, M. J. Marcath, K. Meierbach, L. Nakae, G. Rusev, A. Sood, I. Stetcu, and C. Walker. Correlated prompt fission data in transport simulations. *The European Physical Journal A*, 54(1):9, Jan 2018.
- [6] S. Debenedetti, J. E. Francis, W. M. Preston, and T. W. Bonner. Angular dependence of coincidences between fission neutrons. *Phys. Rev.*, 74:1645–1650, Dec 1948.
- [7] J. S. Pringle and F. D. Brooks. Angular correlation of neutrons from spontaneous fission of ^{252}Cf . *Phys. Rev. Lett.*, 35:1563–1566, Dec 1975.
- [8] J. M. Verbeke, L. F. Nakae, and R. Vogt. Neutron-neutron angular correlations in spontaneous fission of ^{252}Cf and ^{240}Pu . *Phys. Rev. C*, 97:044601, Apr 2018.
- [9] Sara A. Pozzi, Brian Wieger, Andreas Enqvist, Shaun D. Clarke, Marek Flaska, Matthew Marcath, Edward Larsen, Robert C. Haight, and Enrico Padovani. Correlated neutron emissions from ^{252}Cf . *Nuclear Science and Engineering*, 178(2):250–260, 2014.

- 1101 [10] A. M. Gagarski, I. S. Guseva, V. E. Sokolov, G. V. Val'ski, G. A. Petrov, D. O. Krinitzin, D. V. Niko-
 1102 laev, T. A. Zavarukhina, and V. I. Petrova. Neutron-
 1103 neutron angular correlations in spontaneous fission of 252Cf. *Bulletin of the Russian Academy of Sciences, Physics*, 72:773–777, July 2008.
- 1104 [11] V. E. Sokolov and G. A. Petrov. Investigation of the angular dependences of neutron-neutron coincidences from 252Cf, 235U, 233U and 239Pu fission in search of scission neutrons. *Proc. XVIII Internat. Seminar on Interaction of Neutrons with Nuclei (ISSIN-18)*, pages 108–118, 2010.
- 1105 [12] Matthew J. Marcath, Tony H. Shin, Shaun D. Clarke, Paolo Peerani, and Sara A. Pozzi. Neutron angular distribution in plutonium-240 spontaneous fission. *Nuclear Instruments and Methods in Physics Research, Section A: Accelerators, Spectrometers, Detectors and Associated Equipment*, 830:163–169, 9 2016.
- 1106 [13] S Nair, D B Gayther, B H Patrick, and E M Bowey. Fission-neutron and fragment angular distributions from threshold photofission of 232 Th and 238 U. *Journal of Physics G: Nuclear Physics*, 3(7):965, 1977.
- 1107 [14] Jefferson Lab. *CODA 2.6*, 2015.
- 1108 [15] Sara A Pozzi, Enrico Padovani, and Marzio Marseguerra. MCNP-PoliMi: a Monte-Carlo code for correlation measurements. *Nuclear Instruments and Methods in Physics Research Section A: Accelerators, Spectrometers, Detectors and Associated Equipment*, 513(3):550 – 558, 2003.
- 1109 [16] Eric C. Miller, Shaun D. Clarke, Marek Flaska, Sara A. Pozzi, and Enrico Padovani. MCNPX-PoliMi post-processing algorithm for detector response simulations. *JNMM, Journal of the Institute of Nuclear Materials Management*, 40(2):34–41, 12 2012.
- 1110 [17] Lawrence Berkeley National LaboratoryLawrence Livermore National LaboratoryLos Alamos National LaboratoryUniversity of Michigan Nuclear Engineering. *FREYA 2.0.3*, 2016.
- 1111 [18] S. D. Clarke, B. M. Wieger, A. Enqvist, R. Vogt, J. Randrup, R. C. Haight, H. Y. Lee, B. A. Perdue, E. Kwan, C. Y. Wu, R. A. Henderson, and S. A. Pozzi. Measurement of the energy and multiplicity distributions of neutrons from the photofission of ^{235}U . *Phys. Rev. C*, 95:064612, Jun 2017.
- 1112 [19] Krishichayan, M. Bhike, A. P. Tonchev, and W. Tornow. Fission product yield measurements using monoenergetic photon beams. In *European Physical Journal Web of Conferences*, volume 146 of *European Physical Journal Web of Conferences*, page 04018, September 2017.
- 1113 [20] Kyle Cranmer. Kernel estimation in high-energy physics. *Computer Physics Communications*, 136(3):198–207, 2001.